

A Novel 2-D Synthetic Aperture Focusing Technique for Acoustic-Resolution Photoacoustic Microscopy

Seungwan Jeon, *Student Member, IEEE*, Jihoon Park, Ravi Managuli, and Chulhong Kim¹, *Senior Member, IEEE*

Abstract—Acoustic-resolution photoacoustic microscopy (AR-PAM) is a promising technology for vascular or tumor-targeted molecular imaging. Unique advantages of AR-PAM are its non-invasive, non-ionizing real-time, and deeper imaging depth. AR-PAM typically uses an ultrasound transducer with a high acoustic numerical aperture (NA) to enable deeper imaging depth. While high NA achieves good lateral resolution in the focal plane but significantly degrades the lateral resolution in the out-of-focus region. Synthetic aperture focusing technique (SAFT) has been introduced to overcome this out-of-focus degradation by synthesizing the correlated signals. Several 2-D SAFTs have been also reported to improve degraded resolution in all directions. However, the resolution enhancement of the previously reported 2-D SAFTs are suboptimal and are not equivalent to the 1-D SAFT performance under an ideal condition with the sample orientation perpendicular to the synthetic aperture direction. In this paper, we present a new 2-D SAFT called 2-D directional SAFT that improves the lateral resolution significantly and we compare our results against 1-D SAFT under ideal condition. We applied this algorithm to phantom and *in vivo* images to show the improvement in image quality. We also implement this algorithm in a graphical processing unit to achieve high performance to show the practicality of implementing this new algorithm in a system.

Index Terms—Image enhancement/restoration (noise and artifact reduction), microscopy, optoacoustic/photoacoustic imaging, vessels.

I. INTRODUCTION

VASCULAR imaging is an important diagnostic tool to visualize angiogenesis, which is a hallmark of the cancer growth, metastasis, ischemia and tissue degeneration [1]–[4]. Photoacoustic (PA) imaging is a promising vascular imaging technology that can image angiogenesis at a very high resolution without any exogenous contrast agents [5]–[7]. In photoacoustic imaging, the ultrashort-pulsed laser irradiates biological tissue, and transient thermoelastic expansion of the tissue emits ultrasonic waves called PA waves. These generated PA waves are detected by an ultrasound (US) transducer and converted to a PA image of the target [8], [9]. Photoacoustic modality is safe, non-invasive, non-ionizing, and real-time.

In addition to diagnostic imaging, PA microscopy (PAM), based on the same principles as of PA imaging [10], is currently showing potential as a new tool for biomedical research in addition to diagnostic imaging [11], [12]. Amongst several forms of PAM, such as acoustic-resolution PAM (AR-PAM) and optical-resolution PAM (OR-PAM), only AR-PAM with a high numerical aperture (NA) can obtain high-resolution vascular images at a deeper depth. However, it achieves high lateral resolution only near the focal plane and with out-of-focus resolution significantly deteriorated [13], [14]. A novel beamforming technique to improve this out-of-focus resolution is the focus of this paper.

The synthetic aperture focusing technique (SAFT) is one of the ultrasound imaging technique that uses multiple transducer elements to improve the lateral resolution in the image [15]. In 2006, Li *et al.* [16] proposed a method using the SAFT with a virtual detector (VD) concept to overcome the out-of-focus degradation in AR-PAM. Since then several researchers have tried to improve the algorithm further, with the latest publication in 2016 from Park *et al.* [17], and they introduced a more advanced AR-PAM SAFT using delay-multiply-and-sum (DMAS) algorithm.

Now interest in the photoacoustic imaging community is to extend 2D PAM to 3D PAM and thus would require 2D SAFT algorithms. As an extension to 1D SAFT, several

Manuscript received May 14, 2018; accepted June 7, 2018. Date of publication July 31, 2018; date of current version December 28, 2018. This work was supported in part by the Consilience Creative program of the Ministry of Science and ICT (MSIT) supervised by the Institute for Information & communications Technology Promotion (IITP) under grant IITP-2018-2011-1-00783, in part by the Korea Health Technology R&D Project through the Korea Health Industry Development Institute (KHIDI) funded by the Ministry of Health & Welfare under Grant HI15C1817, in part by the NRF Pioneer Research Center Program of the MSIP (MSIT and Future Planning) under Grant NRF-2014M3C1A3017229 and Grant NRF-2017M3C1A3037762, and in part by the National Research Foundation of Korea (NRF) through the Korea Government (MSIP) under Grant 2011-0030075. (Seungwan Jeon and Jihoon Park contributed equally to this work.) (Corresponding author: Chulhong Kim.)

S. Jeon, J. Park, and C. Kim are with the Department of Creative IT Engineering, Pohang University of Science and Technology, Pohang 37673, South Korea (e-mail: jsw777@postech.ac.kr; inventor71@postech.ac.kr; chulhong@postech.edu).

R. Managuli is with the Department of Bioengineering, University of Washington, Seattle 98195 USA, and also with Hitachi Medical Systems of America, Twinsburg, OH 44087 USA (e-mail: ravim@u.washington.edu).

This paper has supplementary downloadable material available at <http://ieeexplore.ieee.org>, provided by the author.

Color versions of one or more of the figures in this paper are available online at <http://ieeexplore.ieee.org>.

Digital Object Identifier 10.1109/TMI.2018.2861400

2D SAFT methods have been proposed to further correct the distorted signals. Generally, the conventional 2D SAFT methods correct delays in the out-of-focus region either in 2-axes (horizontal and vertical) [18] or spherically [19]. However, since the blood vessels have a tubular structure, it is fundamentally difficult to synthesize the PA signal along the actual cylindrical PA wavefront using these 2-axis or spherical SAFTs. Thus, in the process of summing up the delayed signals in 2D SAFTs, unwanted signals get summed up degrading the resolution improvement of the 2D SAFTs resulting in suboptimal 3D volumetric imaging. Because of this problem, the resolution enhancement of the conventional 2D SAFTs was worse than 1D SAFT under the ideal condition where the sample was arranged perpendicularly to the synthesizing direction. Deng *et al.* [20] and Cai *et al.* [21] performed additional adaptive 1D SAFT and deconvolution, respectively, after correcting the image through the existing 2D SAFTs to improve the image resolution further. However, because the additional processes are implemented based on the 2D SAFT output, it is difficult to recover the signal that has already gone away or severely degraded in the 2D SAFT process.

In this study, we have developed a novel 2D-Directional-SAFT (2D-D-SAFT) technique to solve the problem of the conventional 2D SAFTs to reconstruct a 3D volume. Unlike the conventional 2D SAFTs, the proposed 2D-D-SAFT method exclusively synthesizes the signals from the cylindrical wavefronts by merging the corresponding frequency components reinforced by the 1D SAFT in the Fourier domain. We compared the conventional SAFTs and our 2D-D-SAFT quantitatively through phantom and *in vivo* study, and showed the superiority of our technique. Note that our system performs the raster scanning in x and y-axes, and that the x, y, and z-axes denote the horizontal, vertical, and axial directions in this paper. We also implemented this algorithm on GPU for real-time performance.

II. METHOD

We first discuss the conventional 1D and 2D SAFT algorithms. We then present our new Fourier-based 2D-D-SAFT algorithm.

A. Basic of 1D SAFT

In AR-PAM, the SAFT method uses the virtual detector (VD) concept [16], in which a VD is placed at the focus of the transducer. It detects PA signals above and below the geometric focus within a certain solid angle as shown in Fig. 1. With the probe of AR-PAM performing raster scanning, the VD repeatedly detects the PA signal within the PA radiation field in which the solid angle overlaps. 1D SAFT algorithm, based on a delay-and-sum (DAS) algorithm, creates a new A-line by summing up the delayed PA signals detected by neighboring VDs in a specified scanline. The mathematical expression of the DAS-SAFT is as follows:

$$s_{SAFT}(t) = \sum_{i=1}^D s_i(t - \Delta t_i) \quad (1)$$

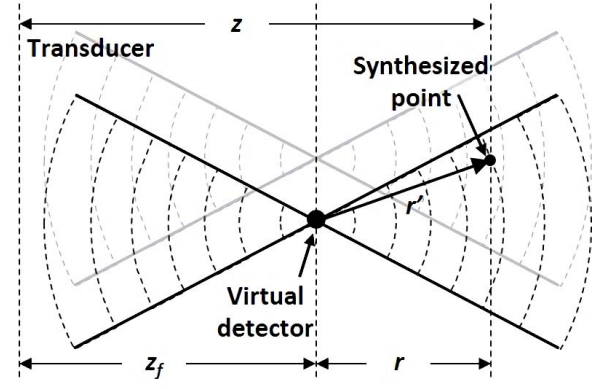


Fig. 1. Diagram of the VD concept in SAFT. VD, virtual detector; z and z_f , the depth of the synthesized point and the VD, respectively; r and r' , the axial and straight distance between synthesized point and VD, respectively.

where s_{SAFT} denotes the synthesized signal, D is the number of the signals to be summed, s_i denotes received signal at i -th scan, and Δt_i is the time delay applied to s_i . D is determined by PA detection range of the VD, related to the NA of the transducer. The time delay, Δt_i , is calculated as follows:

$$\Delta t_i = \text{sgn}(z - z_f) \frac{r - r'}{c} \quad (2)$$

where z and z_f denote the depth of the synthesized point and the VD, respectively, r and r' denote the axial distance and distance between synthesized point and VD, respectively, and c represents the speed of ultrasound in the medium. During raster scanning, distortion of the curvature shape is observed in the unfocused area because the PA signal, from a same source, is repeatedly detected with different time delays depending on the transducer position in the out-of-focus region.

To further improve the focusing quality of the SAFT, side lobes are suppressed by multiplying the channel data with a coherence factor (CF) defined as [16], [22]:

$$CF(t) = \frac{|\sum_{i=1}^D s_i(t - \Delta t_i)|^2}{D \sum_{i=1}^D |s_i(t - \Delta t_i)|^2} \quad (3)$$

This CF is multiplied with the output of SAFT of (1) to effectively suppress the side lobes:

$$s_{SAFT-CF}(t) = CF(t) \cdot s_{SAFT}(t) \quad (4)$$

When the received signals $s_i(t - \Delta t_i)$ are arising from the targets on axis, the signals are coherent and CF is close to one, which will enhance the $s_{SAFT-CF}$. On the contrary, when the target is off axis, the received signals $s_i(t - \Delta t_i)$ are incoherent and CF is close to zero and thus reducing the contribution to $s_{SAFT-CF}$.

B. Conventional 2D SAFT

The 1D SAFT method greatly improves the AR-PAM's focusing capability, but in one direction only. For image enhancement in two directions, two representative 2D SAFT methods have been introduced by Deng *et al.* [18] in 2011 and

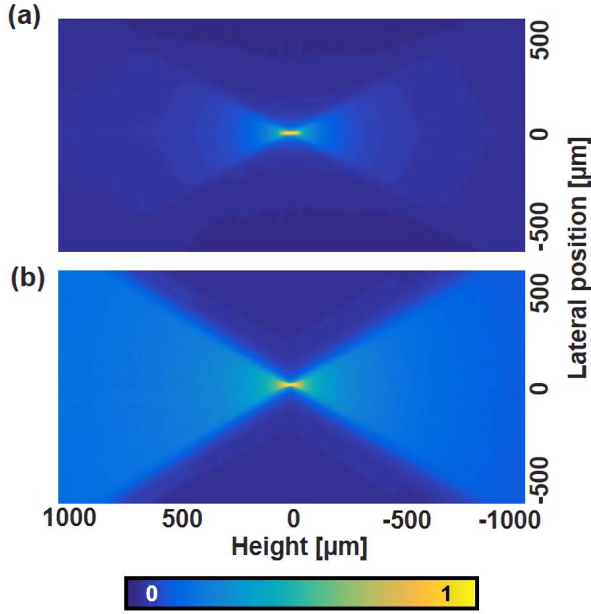


Fig. 2. Spatial Impulse Response (SIR) of a (a) spherical lens and (b) cylindrical lens used as weight functions in 2D-S-SAFT technique.

by Turner *et al.* [19] in 2014. These two methods provide a baseline for comparing the performance against our technique. Deng *et al.* performed the DAS algorithm both horizontally and vertically to correct both directions of the distortion and we refer to this method as 2D Cross SAFT (2D-X-SAFT) in this manuscript. The equation for the 2D-X-SAFT is as follows:

$$s_{2D-X-SAFT}(t) = \sum_{i=1}^D s_i(t - \Delta t_i) + \sum_{j=1}^D s_j(t - \Delta t_j), \quad (5)$$

where s_j denotes a j -th received signal having a time delay, Δt_j , in a direction perpendicular to s_i . The CF of 2D-X-SAFT is calculated as follows:

$$CF(t) = \frac{|\sum_{i=1}^D s_i(t - \Delta t_i) + \sum_{j=1}^D s_j(t - \Delta t_j)|^2}{2D \sum_{i=1}^D [s_i(t - \Delta t_i)^2 + \sum_{j=1}^D s_j(t - \Delta t_j)^2]} \quad (6)$$

This $CF(t)$ is multiplied with the $s_{2D-X-SAFT}$ to obtain the final output.

Turner *et al.* introduced a spatial impulse response based on SAFT (SIR-SAFT) algorithm. This 2D SAFT adds the signals corresponding to a hemispherical-like area and we refer to this as 2D spherical SAFT (2D-S-SAFT) in this study for convenience. The 2D-S-SAFT is expressed as:

$$s_{2D-S-SAFT}(t) = \sum_{i,j=1}^{circle} s_{ij}(t - \Delta t_{ij}) SIR_{ij}(t) \quad (7)$$

where s_{ij} is the signal received within the circle, Δt_{ij} is the time delay applied to s_{ij} , and SIR is a weighting function to rectify the different spatial contribution in SAFT [23]. In this study, we calculated the SIR by simulating it with DREAM toolbox in MATLAB for spherical and cylindrical lenses as

shown in Fig. 2a and 2b. CF of 2D-S-SAFT is modified accordingly to reduce side lobes in 2D-S-SAFT:

$$CF(t) = \frac{|\sum_{i,j=1}^{circle} s_{ij}(t - \Delta t_{ij}) SIR_{ij}(t)|^2}{M \sum_{i,j=1}^{circle} |s_{ij}(t - \Delta t_{ij}) SIR_{ij}(t)|^2} \quad (8)$$

where M is the total number of signals in the synthetic aperture.

As can be seen in equations (5-8), the conventional 2D SAFTs synthesize signals with the corresponding time delays in two orthogonal or all directions. However, blood vessels are tubular in structure and propagate PA waves cylindrically. Thus the conventional methods based upon the assumption that the PA source is a single point is not suitable for synthesizing PA wavefront signals originating from tubular blood vessels. A new algorithm is needed to capture these cylindrical PA waves to generate the 3D images of the vascular structure.

C. Proposed 2D Directional SAFT

The 1D SAFT algorithm can correlate the corresponding signals to achieve better lateral resolution, compared to the other 2D SAFTs, such as Deng *et al.* and Turner *et al.* developed, but in one direction only if it is under the ideal condition. This is because in the cross section perpendicular to the vessel direction, the actual delays of the signals match well with the delays calculated by 1D SAFT. In our technique we extend the advantages of 1D SAFT to 2D SAFT, in where we uniquely merge multiple 1D SAFT to form a 2D image. The proposed 2D-D-SAFT first performs 1D SAFT in several directions, extracts only the improved frequency components from each 1D-SAFT output, and merges the components in the Fourier domain. In the 1D SAFT process, we applied the SIR weighting function to suppress the large amplification in the out-of-focus region as follows:

$$s_{SIR-1D-SAFT,\theta}(t) = \sum_{i=1}^D s_{i,\theta}(t - \Delta t_i) SIR_{i,\theta}(t) \quad (9)$$

where $s_{SIR-1D-SAFT,\theta}(t)$ is the output obtained by performing the 1D SAFT at angle θ in x-y plane, the $s_{i,\theta}(t - \Delta t_i)$ denotes the corresponding signals, and $SIR_{i,\theta}(t)$ denotes the SIR from a cylindrical lens placed at the angle of θ , with impulse response shown in Fig. 2b. We used SIRs simulated with a cylindrical lens in equation (9), even though the AR-PAM is built with a spherical lens. This is because, unlike in 2D-S-SAFT, only signals in a plane contribute to the summation in 1D SAFT.

During the raster scanning of the PAM system, the 3D raw data was acquired by default z-x-y data sequence order. We transposed the data sequence order from z-x-y to x-y-z to apply 2D fast Fourier transform (FFT) on x-y plane of the 1D SAFT outputs. After transposition, data was transformed into Fourier domain as follows:

$$S_\theta(u, v, z) = \mathcal{F}\{s_{SIR-1D-SAFT,\theta}(x, y, z)\} \quad (10)$$

where $s_{SIR-1D-SAFT,\theta}(x, y, z)$ is the enveloped 1D SAFT output after Hilbert transform, and $\mathcal{F}\{s(x, y, z)\}$ represents 2D FFT of $s(x, y, z)$.

Since the resolution improvement of SAFT depends on the synthetic aperture direction, the direction of the frequency extension would be depending on the synthetic aperture direction. Thus, to selectively extract the reinforced high frequency range according to the synthetic aperture direction and combine them to form one image, we merged the Fourier domain images as follows:

$$S_{merged,N}(u, v, z) = \sum_{n=0}^{N-1} (S_n(u, v, z) \cdot M_n(u, v)), \quad (11)$$

where N is the total number of angles used in 2D-D-SAFT and $S_n(u, v, z)$ is the Fourier transformed of 1D SAFT performed at n -angle. $M_n(u, v)$ is an n -th Hanning window to extract the frequency components in a specific angle, $\theta = (n/N)\pi$ rad and is defined as:

$$M_n(u, v) = \begin{cases} \frac{1}{N}, & \text{if } u = \left\lceil \frac{X-1}{2} \right\rceil \text{ and } v = \left\lceil \frac{Y-1}{2} \right\rceil \\ \cos^2\left(\frac{\bar{\theta}_n(u, v) \times N}{2}\right), & \text{if } |\bar{\theta}_n(u, v)| \leq \frac{\pi}{N} \\ 0, & \text{otherwise,} \end{cases} \quad (12)$$

$$\bar{\theta}_n(u, v) = ((\theta + \Delta\theta(u, v)) \bmod \pi) - \frac{\pi}{2}, \quad (13)$$

$$\Delta\theta(u, v) = \text{atan}\left(\frac{v - \left\lceil \frac{Y-1}{2} \right\rceil}{u - \left\lceil \frac{X-1}{2} \right\rceil}\right),$$

$$\Delta\theta(u, v) \in \left(-\frac{\pi}{2}, \frac{\pi}{2}\right),$$

$$u \in (0, X-1), \quad v \in (0, Y-1), \quad (14)$$

where $\lceil a \rceil$ is the ceiling function, and X and Y are the number of pixels in x and y -axes of the image, respectively. To avoid the distortion due to excessive summing of frequency components in $S_{merged,N}(u, v, z)$, we designed $M_n(u, v)$ based on the Hanning window to minimize the side lobes [24] and to satisfy the following conditions:

$$\sum_{n=0}^{N-1} M_n(u, v) = 1. \quad (15)$$

The examples of 2D Hanning window-based mask are shown in Supplementary Fig. 1. Supplementary materials are available in the supplementary files /multimedia tab. We transformed the merged Fourier domain image, $S_{merged,N}(u, v, z)$, into spatial domain by performing inverse Fourier transform as follows:

$$s_{D-SAFT,N}(x, y, z) = \mathcal{F}^{-1}\{S_{merged,N}(u, v, z)\}. \quad (16)$$

The final stage of re-transposing the data to z - x - y order is optional since the data can be rendered in any direction for visualization. However, processing time we presented in TABLE II include the final transposition time as well for the sake of completeness of our technique.

III. RESULT

A. SIR Weighting Function in SAFT

We applied cylindrical lens SIR weighting functions specifically designed for 1D SAFT to our technique because

2D-D-SAFT is a combination of several 1D SAFTs. Note that Turner *et al.* used the spherical lens SIR for 2D-S-SAFT [19]. We created the SIR functions using the MATLAB-based DREAM toolbox and compared the performance of the cylindrical and spherical lens SIR functions in 1D and 2D SAFTs (Fig. 3).

We imaged a skewed single carbon fiber phantom using a commercial PAM system (switchable rapid-scanning PAM system, Microphotoacoustics, USA) with the acoustic NA of 0.5, an ultrasound transducer (V214-BB-RM, Olympus-NDT, USA) centered at 50 MHz, and a pulsed laser (Supplementary Fig. 2) [25] with the energy of 8 μ J/pulse and wavelength of 532 nm. In this investigation, we compared the 1D SAFT with a synthetic aperture perpendicular to the sample direction and 2D spherical SAFT. Note that the positive and negative height implies above and below the focal point, respectively.

In the out-of-focus region, before the application of SAFT, the carbon fiber was blurred in the height-encoded image (Fig. 3b). In both 1D SAFT and 2D-S-SAFT images, the lateral resolution in the out-of-focus improved (red lines in Fig. 3d and 3e) but the contrast in the focal area reduced (Fig. 3c (i) and (iv)) due to the large amplitude of the synthesized signals in the out-of-focus area. When SIR weighting function was employed, we can see in Fig. 3c (iii) and 3d that the large amplifications arising in the out of focus region (yellow and purple lines in Fig. 3d and 3e) are effectively suppressed. The SIR with the spherical lens, especially, could solve the problem of contrast degradation in the near focus region of the 2D-S-SAFT image and maintain smallest SNR changes along the sample height direction (Fig. 3c (iii) and 3d). In the 1D SAFT image, we can also see that the SIR with the cylindrical lens effectively suppressed the large amplification and produced minimum SNR change along the sample height direction (Fig. 3c (v) and yellow line in Fig. 3e). Thus, we applied the cylindrical SIR to 2D-X-SAFT as well as the proposed 2D-D-SAFT to compensate for their SNR because 2D-X-SAFT is also a combination of two 1D SAFTs.

B. Carbon Fiber Phantom Imaging

We imaged the carbon fiber phantom of Fig. 4a to compare the resolution enhancement of the proposed 2D-D-SAFT algorithm. The phantom has two 6- μ m carbon fibers that are skewed and perpendicular to each other (Fig. 4a), and are acoustically focused during imaging at the intersecting point of the two carbon fibers as shown in the height encoded PA image in Fig. 4b.

As described in the Method section, we first performed 1D SAFTs in several directions independently from each other (Fig. 4c (ii-iii)). In this phantom experiment, we used two angles ($N = 2$), and confirmed the resolution change according to the number of angles in the later experiment. The Figs. 4c(ii) and 4c(iii) show the x - y plane of 1D SAFT outputs ($\theta = 0$ and $1/2 \pi$ rad, respectively) at a certain depth. Due to the high directivity of the 1D SAFT, the 1D SAFT improves the spatial resolution only in a certain direction

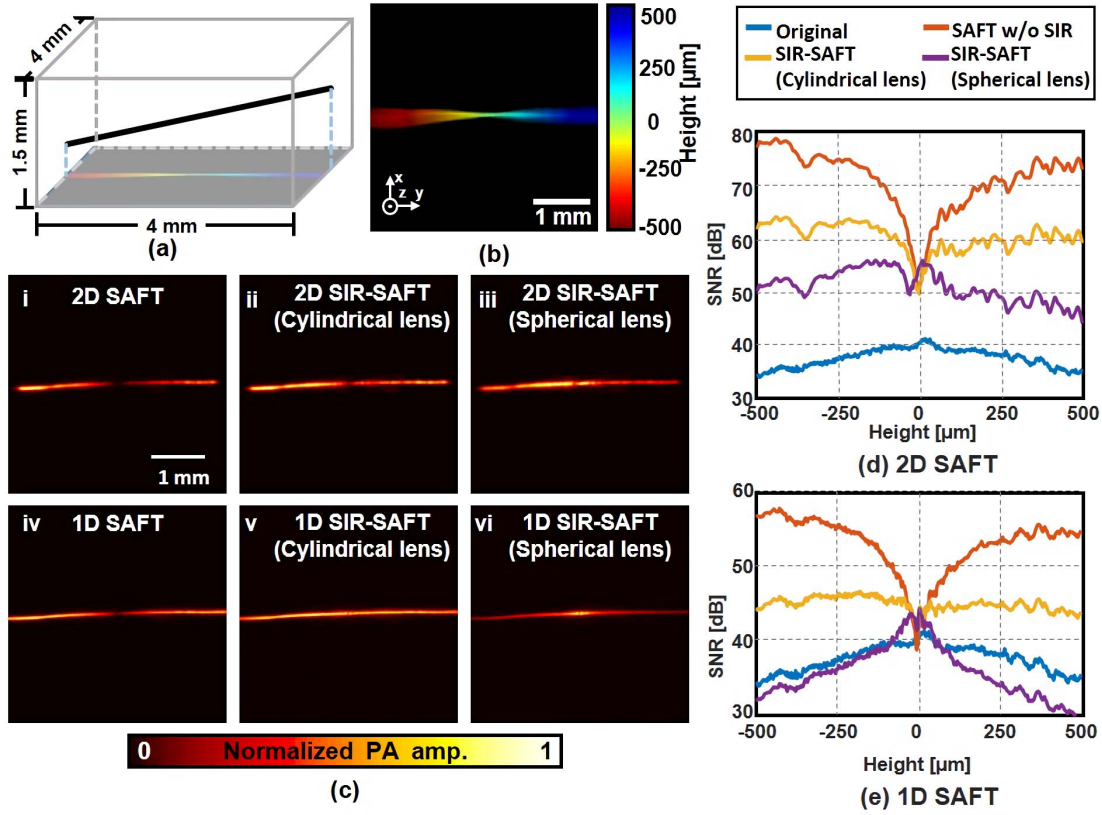


Fig. 3. (a) Diagram of carbon fiber phantom with a 6- μm skewed carbon fiber. (b) Height-encoded PA image of the carbon fiber phantom. (c) Various effect of SIR weighting function in 1D and 2D SAFTs. 2D SAFT images without SIR (i), with SIR from a cylindrical lens (ii) and a spherical lens (iii), and 1D SAFT images without SIR (iv), with SIR from a cylindrical lens (v) and a spherical lens (vi) of the carbon fiber phantom. The SNRs according to the SIR types and sample height in 2D SAFT (d) and 1D SAFT (e). SIR, spatial impulse response; SAFT, synthetic aperture focusing technique; PA, photoacoustic.

according to θ and reinforces the high-frequency signals in that direction (Fig. 4c (iv-v)). We then merged the two 1D SAFT outputs in the Fourier domain (Fig. 4c (vi)) and performed a 2D inverse FFT to reconstruct the 2D-D-SAFT image at every depth along the z-axis (Fig. 4c (vii)) to get the spatial domain information.

To confirm the efficacy of the proposed 2D-D-SAFT, we projected 3D data into 2D projection images using maximum amplitude projection (MAP) algorithm to generate the carbon fiber phantom images along anterior (XY) and lateral (XZ and YZ) directions (Fig. 4d, 4e, and 4f). To demonstrate the performance of our 2D-D-SAFT ($N = 2$) algorithm, we used two 1D SAFTs with θ of 0 (horizontal direction) and $1/2 \pi$ rad (vertical direction). In the 1D SAFT ($\theta = 1/2 \pi$ rad), while the y-axis resolution of the vertically placed carbon fiber improves, the horizontally placed carbon fiber along x-axis still showed blurred signals in the out-of-focus regions (Fig. 4d). Similarly, the 1D SAFT ($\theta = 0$ rad) improved resolution only in horizontal carbon fiber while the vertical fiber remained blurred (Fig. 4e). In contrast, our 2D-D-SAFT algorithm showed improved resolution in both x and y-axes (Fig. 4f), since only the reinforced high-frequency components merged in the frequency domain contribute to image reconstruction.

We quantitatively compared the resolution and SNR enhancement of the proposed 2D-D-SAFT method against

the 1D SAFT and the existing 2D SAFT methods by analyzing the same single carbon fiber phantom (Supplementary Figs. 3 and 4 and Table I). We also evaluated 2D-D-SAFT with several angles, $N \in \{2, 4, 8, 16, 32\}$, to observe the effect of N on the resolution. As mentioned previously, we applied a SIR weighting function from a spherical lens (Fig. 2a) to the 2D-S-SAFT and a SIR weighting function from a cylindrical lens (Fig. 2b) to other SAFT methods. In the focal point, the original and all SAFT images have similar FWHM in the focal point ($\text{FWHM} \leq 62 \mu\text{m}$). However, in the out-of-focus region, the FWHM and SNR were significantly deteriorated in the original image while much improvement can be seen in all SAFT algorithms. The 2D-S-SAFT showed the highest SNR at all sample height since it synthesizes more signals than other SAFT techniques. The two 2D SAFTs, 2D-X-SAFT and 2D-S-SAFT, showed larger SNR change along the sample height ($|\Delta\text{SNR}| \leq 16.2$ and 10.4 dB, respectively) than 1D horizontal SAFT ($|\Delta\text{SNR}| \leq 2.7$ dB). The ΔSNR denotes the difference of SNR. The resolution enhancement of 2D-X-SAFT and 2D-S-SAFT ($\text{FWHM} \leq 99 \mu\text{m}$ and $71 \mu\text{m}$, respectively) was poorer compared to the 1D horizontal SAFT ($\text{FWHM} \leq 62 \mu\text{m}$).

Our 2D-D-SAFT ($N = 2$) showed better resolution improvement ($\text{FWHM} \leq 55 \mu\text{m}$) at all heights compared to conventional 2D SAFTs. When N was 4, the resolution

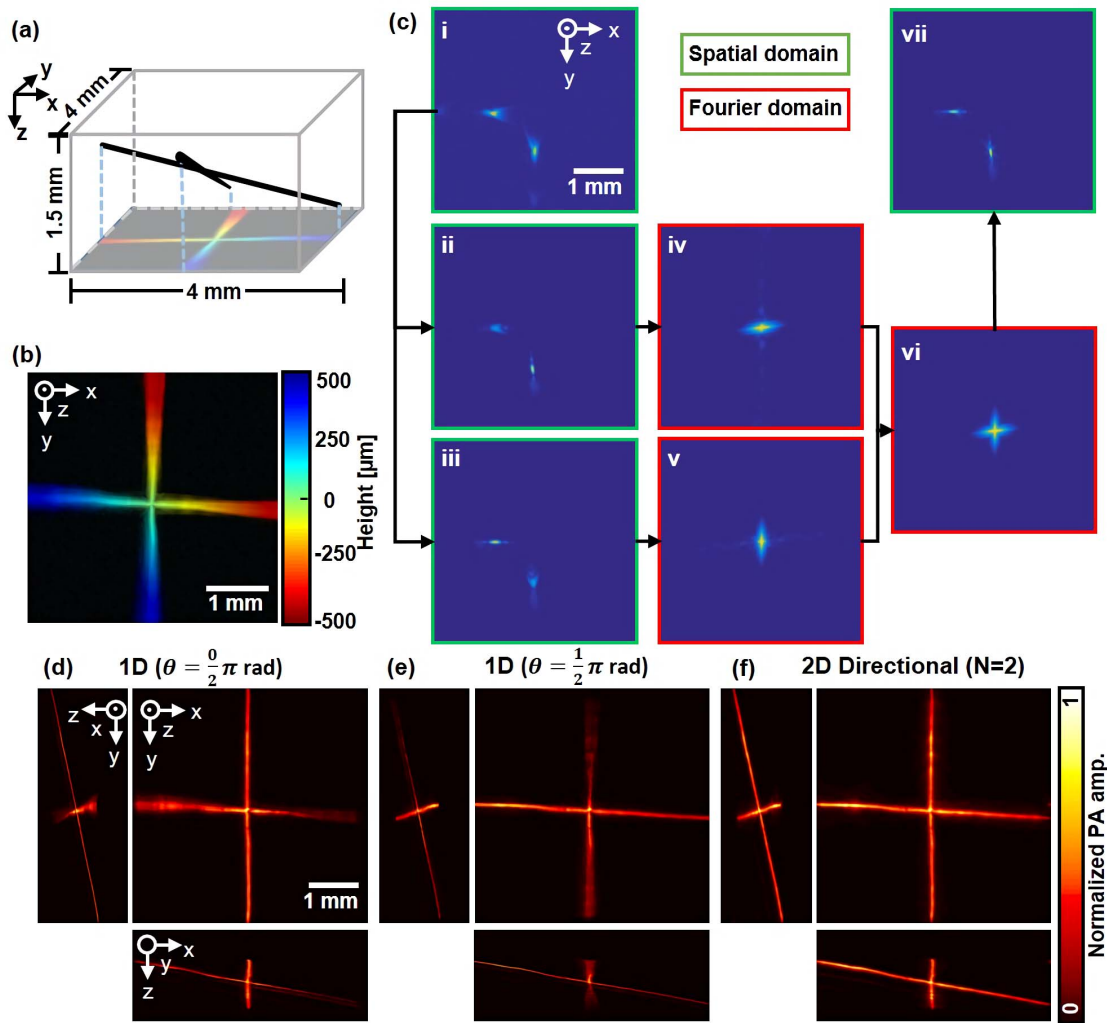


Fig. 4. (a) Diagram of carbon fiber phantom with two 6- μm skewed carbon fibers crossing each other. (b) Height-encoded PA image of the carbon fiber phantom. (c) Image reconstruction process of the 2D directional SAFT ($N = 2$), a sliced plane at a certain height from PA original image (i), 1D SAFT images ($\theta = 0$ and $1/2 \pi$ rad, respectively) in spatial domain (ii and iii) and Fourier domain (iv and v), and the merged image in Fourier domain (vi) and spatial domain (vii). Anterior and lateral PA MAP images of the carbon fiber phantom from 1D SAFT ($\theta = 0$ and $1/2 \pi$ rad) (d and e, respectively), and 2D directional SAFT images ($N = 2$) (f). PA, photoacoustic; MAP, maximum amplitude projection; and SAFT, synthetic aperture focusing technique.

of 2D-D-SAFT was worse ($\text{FWHM} \leq 77 \mu\text{m}$) than when N was 2. However, the resolution gradually improved as N increased and became similar to 1D SAFT at $N = 16$ ($\text{FWHM} \leq 53 \mu\text{m}$) in the out-of-focus region. Likewise, the SNR of 2D-D-SAFT also deteriorated as N increased from 2 to 4 ($36.5 \text{ dB} \leq \text{SNR}$ at $N = 4$), and then gradually improved as N increased thereafter ($41.3 \text{ dB} \leq \text{SNR}$ at $N = 32$).

Since 2D-D-SAFT improves resolution by combining multiple 1D SAFT outputs signals originated from specific angles, the resolution directivity would vary depending on N . In other words, if the samples were placed at different angles, such as $1/4 \pi$ rad instead of 0 or $1/2 \pi$ rad, the 2D-D-SAFT ($N = 2$) may not have the same resolution improvements as shown in TABLE I. To investigate this resolution improvement of 2D-D-SAFT on N , we compared the FWHMs of the same carbon fiber phantom 2D-D-SAFT image by applying various phase shifts, Φ , from 0 rad to $1/4 \pi$ at $1/32 \pi$ rad intervals

(Fig. 5 and Supplementary Fig. 5). For example, if Φ was $2/32 \pi$ rad and N was 2, 2D-D-SAFT combined two 1D SAFT outputs ($\theta = 2/32 \pi$ and $18/32 \pi$ rad). The FWHMs of 2D-D-SAFTs ($N = 2$ and 4) was significantly degraded when Φ was $8/32 \pi$ rad ($\text{FWHM} \leq 207 \mu\text{m}$) and when Φ was $4/32 \pi$ rad ($\text{FWHM} \leq 146 \mu\text{m}$), respectively. When N was 8, 16, and 32, the standard deviation of the FWHM of the 2D-D-SAFT according to the phase shift was less than or equal to 1.2, 0.5, and 0, respectively. We used 2D-D-SAFT ($N = 16$) for the later leaf skeleton phantom and *in vivo* imaging, and provided the detailed reason why we used 16 angles are provided in the Discussion section.

We also compared the processing time of each SAFTs (Table II). We accelerated the computing performance of SAFT using graphics processing unit (GPU; GTX970, NVIDIA, USA). The 1D SAFT ($\theta = 0$ rad) took 2.03 seconds in total, which was fastest amongst all SAFTs. The 2D-S-SAFT took 332.00 seconds in calculation, which was

TABLE I
FWHM AND SNR

	Height [μm]									
	Shallow		250		0		-250		Deep	
	500		500		500		500		500	
	FWHM [μm]	SNR [dB]	FWHM [μm]	SNR [dB]	FWHM [μm]	SNR [dB]	FWHM [μm]	SNR [dB]	FWHM [μm]	SNR [dB]
Original	230	35.4	120	37.9	62	40.4	210	37.2	330	34.5
1D ($\theta = 0$ rad)	52	42.6	50	43.7	62	43.5	49	45.3	53	43.1
2D Cross	99	30.7	58	40.4	61	46.9	98	39.9	99	31.9
2D Spherical	60	44.5	56	49.1	58	54.9	73	53.9	71	50.2
2D Directional (N=2)	46	48.0	51	49.9	55	50.8	51	48.7	48	45.5
2D Directional (N=4)	56	41.3	56	44.2	54	45.7	58	43.2	77	36.5
2D Directional (N=8)	59	42.4	55	45.1	54	46.4	49	45.2	66	38.9
2D Directional (N=16)	52	44.1	52	46.1	53	46.9	45	46.6	53	41.0
2D Directional (N=32)	49	44.1	51	46.0	54	46.7	44	46.5	49	41.3

N = Total number of angles used in 2D directional SAFT

TABLE II
TOTAL PROCESSING TIME [sec]

	Memory copy (Host \leftrightarrow Device)	Calculation	Memory copy (RAM \leftrightarrow HDD)	Data transpose	Total
1D ($\theta = 0/2 \pi$ rad)	0.45	1.58	-	-	2.03
1D ($\theta = 1/2 \pi$ rad)	8.23	1.90	-	-	10.13
2D Cross	8.25	2.74	-	-	10.99
2D Spherical	8.33	332.00	-	-	340.33
2D Directional (N=2)	9.94	10.92	23.09	25.40	69.36
2D Directional (N=4)	19.20	20.82	46.12	39.12	125.26
2D Directional (N=8)	37.11	41.36	94.95	66.22	239.64
2D Directional (N=16)	74.29	82.31	315.58	124.20	596.37
2D Directional (N=32)	148.00	163.79	742.65	270.95	1,325.40

N = Total number of angles used in 2D directional SAFT

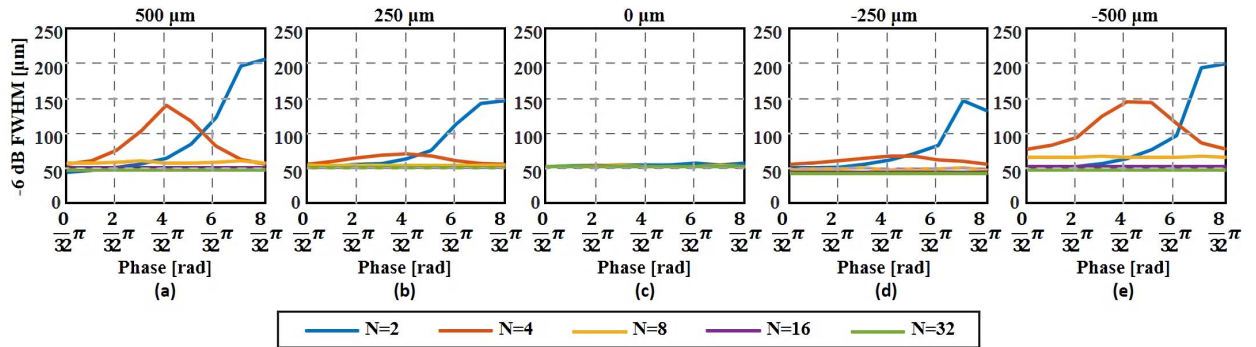


Fig. 5. -6 dB FWHMs of 2D-D-SAFT with various phase shifts at the heights of 500, 250, 0, -250, and -500 μm (a-e, respectively). FWHM, full width at half maximum; 2D-D-SAFT, 2D directional synthetic aperture focusing technique; and N , total number of angles used in 2D-D-SAFT.

the longest amongst SAFTs. However, when $N = 16$ and 32, 2D-D-SAFT had longer total processing time than other SAFT technique because additional overhead required in

transferring and transposing the data. It is because, in the 2D-D-SAFT, we performed 1D SAFT in each angle and stored the 1D SAFT outputs temporarily in off-chip memory

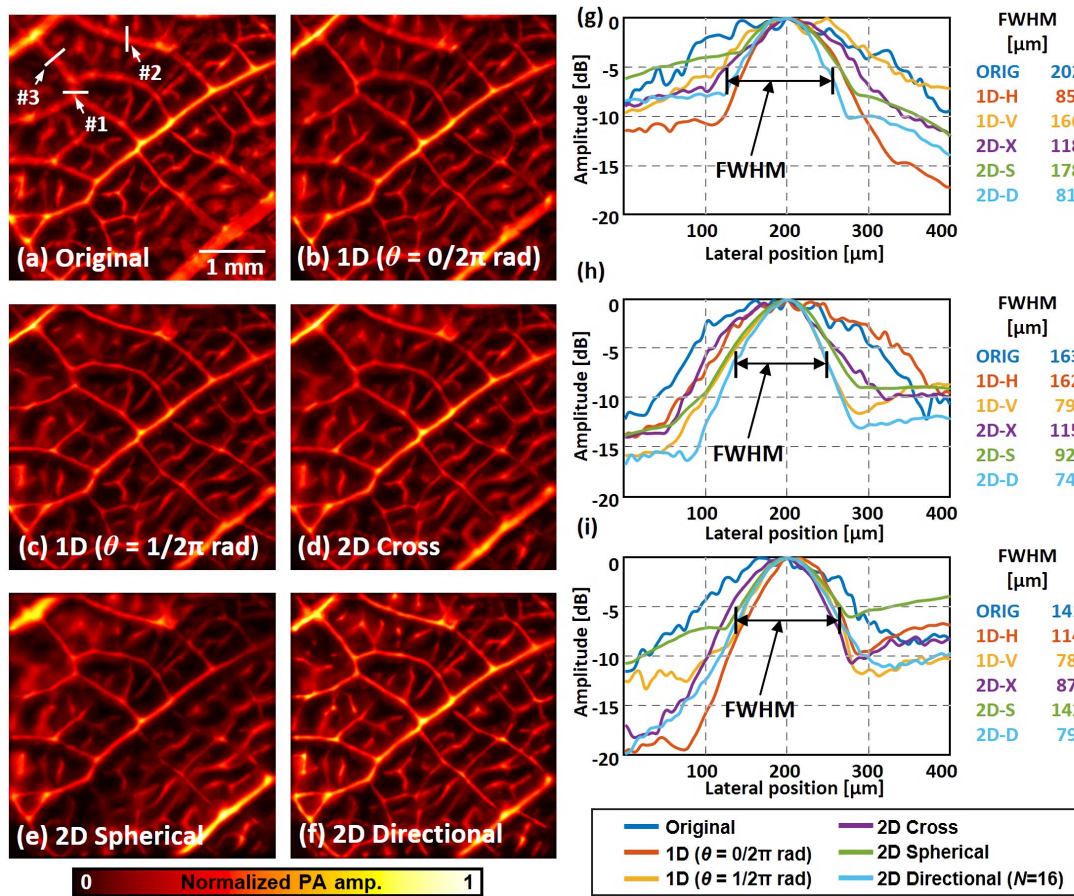


Fig. 6. (a-f) Leaf skeleton phantom MAP images of the original, 1D and 2D SAFTs. (g-i) The line profile, and FWHM from the region highlighted with white lines (#1, #2, and #3, respectively). MAP, maximum amplitude projection; SAFT, synthetic aperture focusing technique; FWHM, full width at half maximum, ORIG, original SAFT, 1D-H, 1D SAFT ($\theta = 0$ rad); 1D-V, 1D SAFT ($\theta = 1/2\pi$ rad); 2D-X, 2D cross SAFT; 2D-S, 2D spherical SAFT; and 2D-D, 2D directional SAFT ($N = 16$).

to effectively utilize limited on-chip memory available on the processor.

C. Leaf Skeleton Phantom Imaging

To see the image quality enhancement of the SAFTs in a sample with a more complex structure, we imaged a leaf skeleton phantom with various sample heights (Fig. 6(a-f) and Supplementary Fig. 6) and analyzed the line-profiles of the sample arranged vertically (Fig. 6g), horizontally (Fig. 6h), and diagonally (Fig. 6i).

Similar to the previous carbon fiber phantom results, 1D-SAFTs ($\theta = 0/2\pi$ and $1/2\pi$ rad) showed smaller FWHM of sample arranged vertically (85 μm ; arrow #1 in Fig. 6a and blue lines in Fig. 6g) and horizontally (79 μm ; arrow #2 in Fig. 6a and blue lines in Fig. 6h), respectively, than the conventional 2D SAFTs. On the other hand, the FWHM of our proposed 2D-D-SAFT was similar (FWHM ≤ 81 μm) in all three directions and was comparable to that of the 1D SAFT as shown in Fig. 6g ($\theta = 0$ rad) and Fig. 6h ($\theta = 1/2\pi$ rad). For diagonally arranged samples, all SAFTs except the 2D-S-SAFT showed improved FWHM

(78 $\mu\text{m} \sim 114$ μm , Fig. 6i) and our 2D-D-SAFT showed almost smallest FWHM of 79 μm .

D. In Vivo Live Animal Imaging

To compare performance of our proposed 2D-D-SAFT against other techniques in an *in vivo* case, we conducted an animal experiment to collect *in vivo* data. The animal experiment was conducted according to the laboratory animal protocol approved by the institutional animal care and use committee of the Pohang University of Science and Technology (POSTECH). In the animal experiment, we anesthetized the mouse by with vaporized 4% isoflurane initially and maintained the anesthesia with 1% isoflurane. We imaged a Balb/c mouse hind limb with a region of interest (ROI) of 12 cm \times 15 cm and with the energy of 16.2 $\mu\text{J}/\text{pulse}$. We used the same acquired data to reconstruct the beamformed image for all SAFT algorithms for performance comparison (Fig. 7 and Supplementary Fig. 7).

In the zoomed original image (Fig. 7a), the blood vessels were blurred globally because the vessels were around 700 μm above the focus and around 300 μm below the skin (Supplementary Fig. 7b and 7c). In this image, it was

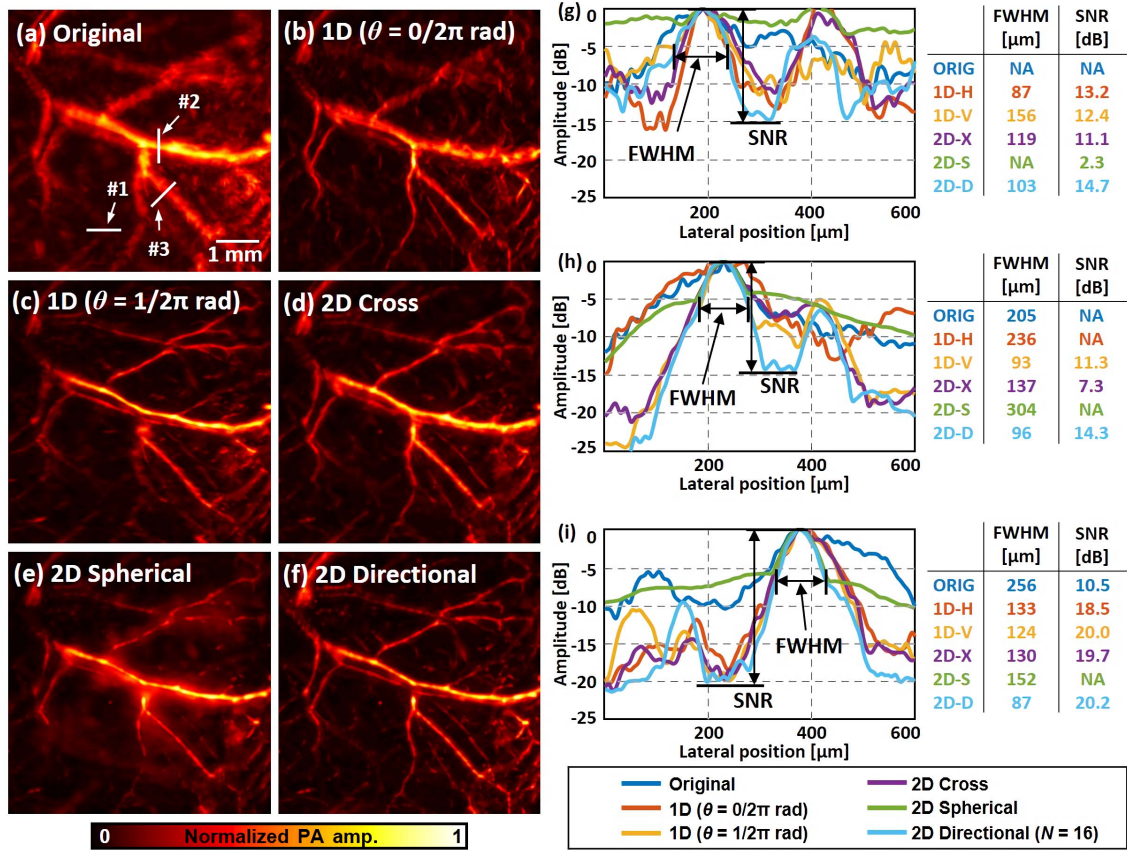


Fig. 7. (a-f) Zoomed mouse hind limb MAP images of the original and 1D and 2D SAFTs. (g-i) The line profile, FWHM, and SNR from the region highlighted with white lines (#1, #2, and #3, respectively). MAP, maximum amplitude projection; FWHM, full width at half maximum; SNR, signal to noise ratio; SAFT, synthetic aperture focusing technique; ORIG, original SAFT, 1D-H, 1D SAFT ($\theta = 0$ rad); 1D-V, 1D SAFT ($\theta = 1/2 \pi$ rad); 2D-X, 2D cross SAFT; 2D-S, 2D spherical SAFT; and 2D-D, 2D directional SAFT ($N = 16$).

difficult to distinguish two separate blood vessels adjacent to each other (arrows #1 and #2 in Fig. 6a and blue line profiles in Fig. 7(g-h)). To compare the effectiveness of SAFT algorithms in this situation, we measured FWHM and SNR of each line profiles (Fig. 7(g-i)). When measuring the SNR, we assumed the lowest amplitude between the two peaks as the noise floor. In this analysis, we did not measure FWHM and SNR if the peak amplitude did not fall below -6 dB until the next peak or if no two peaks could be found. Amongst the 2D SAFTs, the proposed 2D-D-SAFT showed the smallest FWHM (103 μm , 96 μm and 87 μm in vertically, horizontally, and diagonally arranged sample, respectively) and the biggest SNR improvement (14.7 dB, 14.3 dB and 20.2 dB in vertically, horizontally, and diagonally arranged sample, respectively). These FWHM and SNR were comparable to that of the 1D SAFTs under the directionally ideal condition (87- μm FWHM with 13.2-dB SNR and 93- μm FWHM with 11.3-dB SNR in the vertically and horizontally arranged sample, respectively). The other 2D SAFTs were suboptimal compared to 2D-D-SAFT in improving resolution and SNR. In few cases using 2D-S-SAFT, it was difficult to distinguish two adjacent vessels and thus could not measure FWHM or SNR.

IV. DISCUSSION AND CONCLUSION

In the carbon fiber phantom study, we confirmed that the proposed 2D-D-SAFT could successfully improve the lateral

resolution of the images in several directions. 2D-D-SAFT also had slightly improved SNR compared to 1D SAFT, but it could not outperform 2D-S-SAFT regarding SNR. This is because, unlike 2D-D-SAFT, which is based on 1D SAFT, 2D-S-SAFT synthesizes signals from an area rather than a line, resulting in a much lower noise level. However, complicated structures such as the leaf skeleton phantom and the mouse vasculature were blurred in the 2D-S-SAFT images due to the strong side lobes, making it difficult to clearly distinguish the small structures. 2D-X-SAFT had lower side lobes compared 2D-S-SAFT, but had limited resolution improvement compared to 2D-D-SAFT.

The main source of the limitation to improve resolution arises from a mismatch between the actual photoacoustic wavefronts originating from the blood vessels and the synthesized signals directions in the conventional 2D SAFTs. Majority of the blood vessels have a tubular structure thus generating a cylindrical photoacoustic wavefront [18]. This wavefront is not accounted in the conventional 2D SAFTs and the time delays are calculated based on the source to detector distance regardless of the sample shape. In contrast, since 2D-D-SAFT only used well-correlated signals along the SAFT direction, it has resolution improvement similar to that of 1D SAFT under the ideal directional condition. Note that if a higher NA is used, a further improvement in the resolution can be expected since the size of the synthetic aperture receiving the PA signal becomes larger.

We also quantitatively analyzed the effect of the total number of angles used in 2D-D-SAFT on the image since the image quality of the 2D-D-SAFT depends upon the quality of the individual 1D SAFT outputs. Since the resolution enhancement of 1D SAFT has high directivity, the resolution improvement in 2D-D-SAFT also depends on the angle of the sample. We could observe this phenomenon in our experiments with various phase shift (Fig. 5 and Supplementary Fig. 5). In this experiment, instead of acquiring and analyzing samples at various angles, we indirectly reproduced this phenomenon by giving a phase shift to 2D-D-SAFT angle. From the results in Fig. 5, we could infer that the FWHM of the 2D-D-SAFT could be degraded if the angle perpendicular to the sample direction, which is an ideal angle for 1D SAFT, is not used in 2D-D-SAFT. We also can confirm that the directivity of resolution could decrease as the total number of angles of 2D-D-SAFT increases. In addition, we noticed that the total number of angles affected not only the resolution enhancement directivity, but also the resolution enhancement itself. When N was 4, the FWHM of 2D-D-SAFT deteriorated compared to when N was 2. However, FWHM improved again as more angles were used. This is because increasing the number of angles reduced the side lobes, changing the bandwidth at -6 dB (Supplementary Fig. 4). In this analysis, we found that more than 16 angles were required to achieve the resolution improvement similar to that of 1D SAFT.

Previously, several attempts were made to overcome the limitation of the conventional 2D SAFTs. In 2012, Deng *et al.* introduced adaptive SAFT, which performed 1D SAFT in the direction perpendicular to the vessels detected by skeletonization after applying 2D-S-SAFT. Therefore, if the blood vessels were detected appropriately, the resolution enhancement similar to ideal 1D SAFT output could be obtained. We also performed vessels detection and skeletonization in the same manner as [20], but found that some vessels detected by our 2D-D-SAFT were not detected by 2D-S-SAFT. This finding suggests that the adaptive SAFT is cannot always apply 1D SAFT to vessels in proper directions and positions, thus limiting the resolution enhancement. In 2017, Cai *et al.* proposed to use deconvolution after 2D-S-SAFT. Deconvolution is a widely used algorithm in ultrasound [26] and optical imaging [27] for resolution enhancement. We applied the Richardson-Lucy deconvolution to 2D-D-SAFT (Deconvolution-2D-D-SAFT) as well as 2D-S-SAFT (Deconvolution-2D-S-SAFT) in the same way as in [21], and compared their line profiles (Supplementary Fig. 9). As expected, the deconvolution sharpened the vessel edges in both 2D-S-SAFT and 2D-D-SAFT. However, we observed that some vessels could not be distinguished in Deconvolution-2D-S-SAFT, whereas those vessels were well distinguished in Deconvolution-2D-D-SAFT (peaks #1 and #2 in Supplementary Fig. 9c, peaks #1 and #2 in Supplementary Fig. 9d, and peaks #2 in Supplementary Fig. 9e). Thus, we could confirm that the deconvolution technique is more effective in 2D-D-SAFT than in 2D-S-SAFT.

The processing time increased almost linearly with the total number of angles in 2D-D-SAFT. When N was 8 or less, the total processing time was smaller than that of 2D-S-SAFT,

but the processing time was much longer than 1D and 2D-X-SAFT even when N was 2. The main reason for this is that we have to store intermediate 1D SAFT outputs to the off-chip memory because of limited on-chip memory. This I/O overhead was the reason for the degraded performance. This performance could be further improved by utilizing GPUs with larger memory. Performing transpose was the other reason for increased computing time. In this study, we implemented the transpose process using only the central processing unit (CPU), not the GPU, because limited on-chip memory of the GPU used. Thus, in future, we expect to improve the performance of transpose by using a high-performance GPU with the larger memory size.

In this study, we used the switchable OR-PAM and AR-PAM imaging system designed for imaging microcirculation within a shallow depth. Thus, it was equipped with a relatively high center frequency transducer compared to other AR-PAMs [28], [29] limiting the depth of penetration for our *in vivo* experiment to 2 mm. However, our 2D-D-SAFT algorithm could be extended to other PA imaging system with a low center frequency transducer increasing the depth of penetration because the DAS beamforming algorithm, which is used in 2D-D-SAFT, is already widely used in a PA imaging system with a low center frequency transducer [30]. The imaging depth could also be improved further by using high pulse energy even with a 50-Mhz transducer [31]. However, because such a high power laser typically has only a few tens of PRF, fast imaging speed would be challenging. The other reason for the shallow depth is wavelength. We used the wavelength of 532 nm, but this wavelength is highly absorbed by hemoglobin in a biological tissue, making it difficult to penetrate the tissue deeply. Therefore, using a wavelength of around 700 to 900 nm, so called the optical window, can improve the imaging depth [7].

In summary, we developed a novel 2D-D-SAFT to improve the lateral resolution of AR-PAM images in the out of focus region. The proposed 2D-D-SAFT reconstructs an image by merging several 1D SAFT outputs, to overcome the limited resolution enhancement problem of the conventional 2D SAFTs. The 2D-D-SAFT with $N = 32$ showed the smallest resolution directivity and the best resolution enhancement, but compared to 2D-D-SAFT with $N = 16$, those improvements were not that significant and the speed was almost 2x times slower. We could also achieve almost isotropic resolution in the x-y plane and its resolution enhancement was similar to that of 1D SAFT under the ideal condition. Thus, we believe that using 16 angles is most optimal for 2D-D-SAFT. In the leaf skeleton phantom and *in vivo* imaging study, we successfully demonstrated the superior visibility of 2D-D-SAFT over the conventional 2D SAFTs. Thus, we believe that our algorithm could potentially enhance the understanding and research of microvascular circulation due to the improvement in the quality of vascular images.

ACKNOWLEDGMENT

The authors acknowledge Seonghee Cho for fruitful discussions about the beamforming algorithm.

REFERENCES

- [1] M. Toi *et al.*, "Visualization of tumor-related blood vessels in human breast by photoacoustic imaging system with a hemispherical detector array," *Sci. Rep.*, vol. 7, Feb. 2017, Art. no. 41970.
- [2] P. Vajkoczy, A. Ullrich, and M. D. Menger, "Intravital fluorescence videomicroscopy to study tumor angiogenesis and microcirculation," *Neoplasia*, vol. 2, pp. 53–61, Jan./Apr. 2000.
- [3] S. Jeon *et al.*, "In vivo photoacoustic imaging of anterior ocular vasculature: A random sample consensus approach," *Sci. Rep.*, vol. 7, Jun. 2017, Art. no. 4318.
- [4] Y. Zhang *et al.*, "Non-invasive multimodal functional imaging of the intestine with frozen micellar naphthalocyanines," *Nature Nanotechnol.*, vol. 9, pp. 631–638, Jul. 2014.
- [5] J. Kim, D. Lee, U. Jung, and C. Kim, "Photoacoustic imaging platforms for multimodal imaging," *Ultrasonography*, vol. 34, pp. 88–97, Apr. 2015.
- [6] V. Neuschmelting *et al.*, "Performance of a multispectral optoacoustic tomography (MSOT) system equipped with 2D vs. 3D handheld probes for potential clinical translation," *Photoacoustics*, vol. 4, pp. 1–10, Mar. 2016.
- [7] L. V. Wang and S. Hu, "Photoacoustic tomography: In vivo imaging from organelles to organs," *Science*, vol. 335, pp. 1458–1462, Mar. 2012.
- [8] C. Kim, C. Favazza, and L. V. Wang, "In vivo photoacoustic tomography of chemicals: High-resolution functional and molecular optical imaging at new depths," *Chem. Rev.*, vol. 110, pp. 2756–2782, May 2010.
- [9] M. Jeon and C. Kim, "Multimodal photoacoustic tomography," *IEEE Trans. Multimedia*, vol. 15, no. 5, pp. 975–982, Aug. 2013.
- [10] C. Kim *et al.*, "Objective-free optical-resolution photoacoustic microscopy," *J. Biomed. Opt.*, vol. 18, p. 010501, Dec. 2012.
- [11] M. Jeon, J. Kim, and C. Kim, "Multiplane spectroscopic whole-body photoacoustic imaging of small animals in vivo," *Med. Biol. Eng. Comput.*, vol. 54, pp. 283–294, Mar. 2016.
- [12] X. L. Deán-Ben, S. Gottschalk, B. M. Larney, S. Shoham, and D. Razansky, "Advanced optoacoustic methods for multiscale imaging of in vivo dynamics," *Chem. Soc. Rev.*, vol. 46, pp. 2158–2198, Mar. 2017.
- [13] J. Yao and L. V. Wang, "Photoacoustic microscopy," *Laser Photon. Rev.*, vol. 7, pp. 758–778, Sep. 2013.
- [14] S. Park, C. Lee, J. Kim, and C. Kim, "Acoustic resolution photoacoustic microscopy," *Biomed. Eng. Lett.*, vol. 4, no. 3, pp. 213–222, 2014.
- [15] C. H. Frazier and W. D. O'Brien, "Synthetic aperture techniques with a virtual source element," *IEEE Trans. Ultrason., Ferroelectr., Freq. Control*, vol. 45, no. 1, pp. 196–207, Jan. 1998.
- [16] M.-L. Li, H. F. Zhang, K. Maslov, G. Stoica, and L. V. Wang, "Improved in vivo photoacoustic microscopy based on a virtual-detector concept," *Opt. Lett.*, vol. 31, no. 4, pp. 474–476, 2006.
- [17] J. Park, S. Jeon, J. Meng, L. Song, J. S. Lee, and C. Kim, "Delay-multiply-and-sum-based synthetic aperture focusing in photoacoustic microscopy," *J. Biomed. Opt.*, vol. 21, no. 3, p. 036010, 2016.
- [18] Z. Deng, X. Yang, H. Gong, and Q. Luo, "Two-dimensional synthetic-aperture focusing technique in photoacoustic microscopy," *J. Appl. Phys.*, vol. 109, p. 104701, Mar. 2011.
- [19] J. Turner, H. Estrada, M. Kneipp, and D. Razansky, "Improved optoacoustic microscopy through three-dimensional spatial impulse response synthetic aperture focusing technique," *Opt. Lett.*, vol. 39, no. 12, pp. 3390–3393, 2014.
- [20] Z. Deng, X. Yang, H. Gong, and Q. Luo, "Adaptive synthetic-aperture focusing technique for microvasculature imaging using photoacoustic microscopy," *Opt. Express*, vol. 20, no. 7, pp. 7555–7563, 2012.
- [21] D. Cai, Z. Li, Y. Li, Z. Guo, and S.-L. Chen, "Photoacoustic microscopy in vivo using synthetic-aperture focusing technique combined with three-dimensional deconvolution," *Opt. Express*, vol. 25, no. 2, pp. 1421–1434, 2017.
- [22] K. W. Hollman, K. W. Rigby, and M. O'Donnell, "Coherence factor of speckle from a multi-row probe," in *Proc. IEEE Ultrason. Int. Symp.*, Oct. 1999, pp. 1257–1260.
- [23] B. Piwakowski and B. Delannoy, "Method for computing spatial pulse response: Time-domain approach," *J. Acoust. Soc. Amer.*, vol. 86, no. 6, pp. 2422–2432, 1989.
- [24] A. V. Oppenheim and R. W. Schaffer, *Discrete-Time Signal Processing*. London, U.K.: Pearson Educ., 1999.
- [25] S. Hu, K. Maslov, and L. V. Wang, "Second-generation optical-resolution photoacoustic microscopy with improved sensitivity and speed," *Opt. Lett.*, vol. 36, no. 7, pp. 1134–1136, Apr. 2011.
- [26] C. Yu, C. Zhang, and L. Xie, "A blind deconvolution approach to ultrasound imaging," *IEEE Trans. Ultrason., Ferroelectr., Freq. Control*, vol. 59, no. 2, pp. 271–280, Feb. 2012.
- [27] Y. Liu, Y. Liang, G. Mu, and X. Zhu, "Deconvolution methods for image deblurring in optical coherence tomography," *J. Opt. Soc. Amer. A, Opt. Image Sci.*, vol. 26, no. 1, pp. 72–77, 2009.
- [28] H. F. Zhang, K. Maslov, G. Stoica, and L. V. Wang, "Functional photoacoustic microscopy for high-resolution and noninvasive in vivo imaging," *Nature Biotechnol.*, vol. 24, pp. 848–851, Jun. 2006.
- [29] E. W. Stein, K. Maslov, and L. V. Wang, "Noninvasive, in vivo imaging of the mouse brain using photoacoustic microscopy," *J. Appl. Phys.*, vol. 105, no. 10, p. 102027, 2009.
- [30] S. Park, S. R. Aglyamov, and S. Emelianov, "10A-5 beamforming for photoacoustic imaging using linear array transducer," in *Proc. IEEE Ultrason. Symp.*, Oct. 2007, pp. 856–859.
- [31] K. Maslov, G. Stoica, and L. V. Wang, "In vivo dark-field reflection-mode photoacoustic microscopy," *Opt. Lett.*, vol. 30, no. 6, pp. 625–627, 2005.